



Published in final edited form as:

*Opt Express*. 2008 October 27; 16(22): 17530–17541.

## Oxygen Advection and Diffusion in a Three Dimensional Vascular Anatomical Network

Qianqian Fang<sup>1</sup>, Sava Sakadžić<sup>1</sup>, Lana Ruvinskaya<sup>1</sup>, Anna Devor<sup>1,2</sup>, Anders M. Dale<sup>2</sup>, and David A. Boas<sup>1,\*</sup>

<sup>1</sup>*Martinos Center for Biomedical Imaging, Massachusetts General Hospital, 149 13th St, Charlestown, Massachusetts, 02129, USA*

<sup>2</sup>*Department of Neurosciences, University of California, San Diego, CA, USA*

### Abstract

There is an increasing need for quantitative and computationally affordable models for analyzing tissue metabolism and hemodynamics in microvascular networks. In this work, we develop a hybrid model to solve for the time-varying oxygen advection-diffusion equation in the vessels and tissue. To obtain a three-dimensional temporal evolution of tissue oxygen concentration for realistic complex vessel networks, we used a graph-based advection model combined with a finite-element based diffusion model and an implicit time-advancing scheme. We validated this algorithm for both static and dynamic conditions. We also applied it to a complex vascular network obtained from a rodent somatosensory cortex. Qualitative agreement was found with *in-vivo* experiments.

### 1. Introduction

Numerous optical methods are utilized to quantify tissue blood flow, blood volume, and oxygen delivery, ranging from the macroscopic whole tissue level to the microscopic capillary network level and sub-cellular level. Near-infrared spectroscopy (NIRS) and imaging utilize near-infrared light to quantify the concentrations of oxygenated and deoxygenated hemoglobin over cubic centimeters of tissue [1-3]. Visible light tissue reflectance imaged with a CCD camera is frequently used to image superficial changes in hemoglobin concentrations with light spectroscopy [4] and blood flow with laser speckle contrast [5,6], particularly in the neurosciences. Confocal and multiphoton microscopy enable sub-micrometer resolution with depth penetration of up to ~100  $\mu\text{m}$  and ~500  $\mu\text{m}$  or more, respectively, and are used to image the three-dimensional (3D) vascular anatomy and red blood cell velocity within vessels [7,8], and oxygenation of the blood [9-11]. Doppler optical coherence tomography is enabling rapid volumetric imaging of flow within the vascular network over potentially cubic millimeters in seconds [12-14]. There seems to be a unique opportunity for optics to provide a detailed characterization of oxygen delivery to the tissue by combining these measurements of blood flow, volume, and oxygenation with fluorescence-based measurements of cellular activity [15,16] and metabolism [17,18].

The advanced analysis of near-infrared spectroscopy data from centimeters of tissue and visible light imaging from hundreds of micrometers of tissue are yielding information about oxygen metabolism [19-23]. While these estimates of oxygen metabolism appear precise, validating the accuracy is challenged by the lack of a gold standard method. On the other hand, the

\*Corresponding author: E-mail: dboas@nmr.mgh.harvard.edu.

OCIS codes: (180.6900) Three-dimensional microscopy.

microscopic measures of individual microvessels and surrounding tissue provide more direct measures of oxygen delivery, but detailed models are needed to provide an analysis framework to quantify physiological parameters like vessel wall oxygen permeability, tissue oxygen diffusion, and oxygen consumption that are not directly measurable. Further, due to the time varying nature of oxygen delivery, particularly during brain activity, there is a need for models that can handle dynamic, time-varying processes.

In this paper, we describe a detailed computational model of tissue oxygen delivery by a microvascular network that will provide a framework for analyzing multimodal microscopic measures to better quantify additional physiological parameters, and will enable more detailed and realistic analyses of the accuracy of near-infrared spectroscopy and visible light imaging. We start by describing our method for solving the time-varying oxygen advection diffusion equation that estimates velocity within individual microvessel segments, oxygen flux across the permeable vascular walls, and then oxygen diffusion and consumption within the tissue. After validating our solver, we demonstrate its application by calculating oxygen delivery by a microvascular network acquired in rodent somatosensory cortex by two-photon microscopy over a  $230 \times 230 \times 450 \mu\text{m}^3$  volume of tissue.

## 2. Methods

### 2.1 Models and Domain Discretization

The transport and consumption of oxygen in the vessel network and tissue are characterized by the advection-diffusion equation [24], which can be expressed as the following equations:

$$\frac{\partial C_T}{\partial t} = \vec{v} \cdot \nabla C_F - \vec{v} \cdot \nabla C_B + \nabla \cdot (D_{O_2} \nabla C_F) - OC, \quad (1)$$

$$C_B = 4C_{Hb} HSO_2(C_F), \quad (2)$$

where  $C_F$  and  $C_B$  are the free and bounded oxygen concentrations ( $\mu\text{M}$ ), respectively;  $C_T = C_B + C_F$  denotes the total oxygen concentration,  $\vec{v}$  denotes the velocity (m/s),  $D_{O_2}$  is the oxygen diffusion coefficient ( $\text{m}^2/\text{s}$ ), and  $OC$  is the tissue oxygen consumption rate ( $\mu\text{M}/\text{s}$ ). Equation (2) denotes the equilibrium between the hemoglobin bound oxygen and free oxygen where  $H$  denotes hematocrit,  $C_{Hb}$  is the hemoglobin concentration within a red blood cell,  $SO_2(C_F)$  is the hemoglobin oxygen saturation and it is in equilibrium with the concentration of free oxygen,  $C_F$ , as described by the oxygen disassociation curve. We use an invertible form for the oxygen disassociation curve given by [25]. We note that under physiological conditions, all of these parameters can vary in space and time.

Certainly, one could solve Eq. (1) using a single numerical approach, such as a finite element (FE) or a finite difference (FD) method, by applying a full spatial discretization of the tissue volume, the exterior surface and the interior volume of vessels. Because of the small length-scale of the vessel wall, the meshing and computational expense can be prohibitive with increasing complexity of the vessel networks. Instead, we devised a hybrid model that includes a graph-based one-dimensional (1D) oxygen advection model within the vessel, a 1D oxygen flux conservation model across the vessel wall, and an FE-based 3D oxygen diffusion model within the tissue. An implicit (Crank-Nickson) [26] scheme was implemented to compute the updates at each time step. A schematic of the problem domain decomposition and our spatial

discretization scheme is shown in Fig. 1. The computational space is separated into three domains to characterize three distinct physical and physiological processes:

- I. vessel network:** inside the vessel, the oxygen transport is represented by the advection equation subject to the equilibrium of the free and hemoglobin bound oxygen:

$$\begin{aligned}\frac{\partial C_F}{\partial t} &= -\vec{v} \cdot \nabla C_F, \\ \frac{\partial C_B}{\partial t} &= -\vec{v} \cdot \nabla C_B, \\ C_B &= 4C_{\text{Hb}} HS O_2(C_F).\end{aligned}\quad (3)$$

An oriented graph representation was created to represent the vessel network: the axial line of each vessel was extracted and discretized by nodes and oriented edges (see Fig. 1). The connection (including branches) of the vessel network can be naturally expressed by the adjacency matrix [27] of the graph. We calculated a vessel volume associated with each vessel node and assumed uniform oxygen distribution within the volume.

- II. vessel wall:** the oxygen flux across a thin vessel wall is a diffusion process. To simplify analysis, we only discretized the exterior of vessel walls by a triangular surface mesh. Because the diffusion profile within the vessel wall layer is not the primary interest of this study, we used an oxygen conversation relationship based on Fick's law [28]:

$$\frac{\partial C_{F,i}}{\partial t} V_i = J_i A_i, \quad (4)$$

where  $J_i$  is the oxygen flux (mol/m<sup>2</sup>/s) across the vessel wall at the  $i^{\text{th}}$  vessel wall node,  $A_i$  and  $V_i$  are the associated vessel wall area and tissue volume for this node. The right-hand-side of Eq. (4) represents the extracted oxygen from the vessel per unit time. The flux,  $J_i$ , is computed by

$$J_i = -K_w \frac{(C_{F,i} - C_{F,i0})}{\alpha w}, \quad (5)$$

where  $K_w$  is the vessel wall permeability,  $w$  is the vessel wall thickness,  $C_{F,i}$  and  $C_{F,i0}$  are the free oxygen concentrations at the exterior and interior surfaces of the vessel, respectively;  $\alpha$  is the Bunsen solubility coefficient and equals  $1.27 \times 10^{-15}$   $\mu\text{mol}/(\mu\text{m}^3 \text{ mmHg})$  [28].

- III. tissue:** the free oxygen that is transferred across the vessel wall diffuses through the whole tissue volume governed by the diffusion equation

$$\frac{\partial C_F}{\partial t} = \nabla \cdot (D_{O_2} \nabla C_F) - OC, \quad (6)$$

where  $D_{O_2}$  is the tissue oxygen diffusion coefficient and the consumption of oxygen is governed by OC. The tissue volume is discretized by a tetrahedron mesh and is truncated by a bounding box.

In the following subsections, we detail our numerical implementation for solving the above models for each domain.

**Vessel Blood Advection**—Equation (3) is solved in two steps for each time advance. We first solve the two advection equations in Eq. (3). Integrated within the associated volume of each vessel node, the advection equations lead to the conservation equations of free and bound oxygen. Assuming that the adjacency matrix for the vessel graph is  $K$ , for the  $i^{\text{th}}$  vessel node (excluding the vessel end nodes) the conservation of oxygen implies that

$$\frac{\partial C_i}{\partial t} V_i = - \sum_{j=1}^{N_v} k_{i,j} v_{i,j} \frac{C_i V_i - C_j V_j}{d_{i,j}}, \quad (7)$$

where  $N_v$  is the total number of vessel nodes;  $k_{i,j}$  is the  $(i,j)^{\text{th}}$  element of  $K$  with a value of 0 if nodes  $i$  and  $j$  are not adjacent, 1 for in-flow from node  $j$  to  $i$ , and -1 for out-flow from node  $i$  to  $j$ ;  $d_{i,j}$  is the distance between the  $i^{\text{th}}$  and  $j^{\text{th}}$  nodes and  $C_i$  and  $C_j$  are the oxygen concentrations (free or hemoglobin bound);  $v_{i,j}$  is the velocity,  $V_i$  and  $V_j$  are the associated vessel volumes of the two nodes. An implicit finite difference scheme is used for the time-derivative term in (7). This results in a linear equation with a form of

$$\frac{1}{\Delta t} V_i C_i^{n+1} + \sum_j \frac{\theta k_{i,j} v_{i,j}}{d_{i,j}} (V_i C_i^{n+1} - V_j C_j^{n+1}) = \frac{1}{\Delta t} V_i C_i^n - \sum_j \frac{(1-\theta) k_{i,j} v_{i,j}}{d_{i,j}} (V_i C_i^n - V_j C_j^n), \quad (8)$$

where  $\theta \in [0,1]$  is a constant,  $\Delta t$  is the time step and  $n$  is the time index. This can be rewritten in matrix form as

$$\begin{aligned} A_a C_F^{n+1} &= B_a C_F^n, \\ A_a C_B^{n+1} &= B_a C_B^n. \end{aligned} \quad (9)$$

The equilibrium of  $C_F$  and  $C_B$  is achieved by solving

$$C_B^{n+1} = 4 C_{Hb} H S O_2 (C_F^{n+1}), \quad (10)$$

subject to the conservation of  $C_T$ .

**Oxygen Flux Across Vessel Wall**—From Eq.(4), we can get

$$\frac{\partial C_{F,i}}{\partial t} = - K_w \frac{(C_{F,i} - C_{F,0}) A_i}{\alpha w V_i}, \quad (11)$$

which can be converted into an implicit time update as

$$\frac{1}{\Delta t} C_{F,i}^{n+1} + \frac{\theta K_w A_i}{awV_i} (C_{F,i}^{n+1} - C_{F,i_0}^{n+1}) = \frac{1}{\Delta t} C_i^n - \frac{(1-\theta)K_w A_i}{awV_i} (C_{F,i}^n - C_{F,i_0}^n), \quad (12)$$

The matrix form of Eq. (12) can be written as a linear equation defined between the vessel wall and axial nodes:

$$A_f C_F^{n+1} = B_f C_F^n. \quad (13)$$

**Tissue Oxygen Diffusion**—To accommodate for the arbitrary shape of a complex vessel network, we used a tetrahedral mesh to discretize the tissue region outside the vessel. A finite element method (FEM) coupled with implicit time-stepping is used to solve for the diffusion of oxygen in the tissue.

Using the Galerkin's method, the FEM weak form of Eq. (6) can be written as [26]

$$\sum_{i=1}^4 \frac{\partial C_i}{\partial t} \langle \varphi_i, \varphi_j \rangle + \sum_{i=1}^4 C_i \langle D_{O_2} \nabla \varphi_i, \nabla \varphi_j \rangle = \oint_{\partial \Omega} D_{O_2} \nabla C \cdot \hat{n} \varphi_i ds + \langle OC, \varphi_i \rangle, \quad (14)$$

where  $\varphi_i$  and  $\varphi_j$  are the basis functions in a tetrahedral element;  $\partial \Omega$  is the surface of the tissue, and  $\hat{n}$  is a unit vector pointing to the normal direction of a surface element;  $\langle \bullet \rangle$  denotes volume integration inside an element. After applying the implicit method to discretize the time derivative in Eq. (14), we obtain

$$A_d C_F^{n+1} = B_d C_F^n + \mathbf{R}, \quad (15)$$

where the elements of matrices  $A_d$  and  $B_d$  and vector  $\mathbf{R}$  are, respectively, defined by

$$\begin{aligned} a_{i,j} &= \langle \varphi_i, \varphi_j \rangle + \theta \langle D_{O_2} \nabla \varphi_i, \nabla \varphi_j \rangle, \\ b_{i,j} &= \langle \varphi_i, \varphi_j \rangle + (1-\theta) \langle D_{O_2} \nabla \varphi_i, \nabla \varphi_j \rangle, \\ r_i &= \int_k^{k+1} \left( \oint_{\partial \Omega} D_{O_2} \nabla C \cdot \varphi_i \hat{n} ds + \langle OC, \varphi_i \rangle \right) dt. \end{aligned}$$

**Lumped System**—The discretized advection equation, Eq. (9), flux equation, Eq. (13) and diffusion equation, Eq. (15), are defined on the vessel axial nodes, vessel surface/axial nodes and vessel surface/tissue nodes, respectively. In order to solve the entire domain, we can assemble these equations into a lumped system by assigning a global index for the nodes located in three regions. Because of the nonlinear nature of Eq. (10), we solve for the advection separately. We combine Eq. (13) and Eq. (15) as

$$(A_f + A_d) C^{n+1} = (B_f + B_d) C^n + \mathbf{R}. \quad (16)$$

Then, we solve for the time evolution of the oxygen concentration (including both free and hemoglobin bound oxygen) by solving Eqs. (9), (10), and (16) sequentially.

We also note that the unconditional stability of implicit time-stepping may no longer hold due to the presence of Eq. (10). A rigorous derivation of the stability condition for this model is beyond the scope of this paper. We confirmed the stability of our solution by obtaining identical solutions with smaller time steps.

**Boundary Conditions**—Equations (9) and (16) must be solved with proper boundary conditions. The boundary nodes include all the nodes on the exterior surface of the domain, which are either tissue surface nodes or the in-flow/out-flow vertices of vessel axes. For the tissue surface nodes, we used a mirror boundary condition. i.e.

$$\nabla C|_{\partial\Omega}=0. \quad (17)$$

This effectively eliminates the surface integration term in Eq. (14) and the expression for the elements of the vector  $\mathbf{R}$  is simplified to

$$r_i = \langle OC, \varphi_i \rangle \Delta t.$$

For the vessel axes end nodes, the flow rates at all in-flow peripheral points are specified (type-1 boundary condition) and a sink condition is used for the out-flow peripheral points.

## 2.2 Two-photon microscopy measurements of rodent microvasculature network

Sprague Dawley rats (250-320 g) were initially anesthetized with isoflurane and ventilated with a mixture of air and oxygen during surgical procedures. Cannulas were inserted in the femoral artery and vein and heart rate, blood pressure, body temperature and blood gases were monitored. A cranial window 3 mm × 3 mm in size was opened in the parietal bone and dura was removed. The window was filled with agarose and sealed with a coverslip. During the measurement isoflurane was discontinued and anesthesia was maintained with 50 mg/kg intravenous bolus of alpha-chloralose followed by continuous intravenous infusion at 40 mg/(kg h). All experimental procedures were approved by the Massachusetts General Hospital Subcommittee on Research Animal Care.

Blood plasma was labeled with Dextran-conjugated fluorescein (FD 2000S, Sigma-Aldrich; 500 nM concentration in blood). Imaging of the cortical vasculature was performed with a two-photon microscope (Ultima, Prairie Technology Inc.) at 800 nm and with an Olympus 40X water immersion objective ( $NA = 0.8$ ). The individual 256 × 256 pixels frames in the  $X$ - $Y$  planes perpendicular to the optical axis spanned 230 μm × 230 μm. They were obtained as an average of four images in order to smooth the appearance of the red blood cells (not labeled with the dye) and to improve further image analysis. The step size between frames along the optical axis was set to  $\Delta z = 1$  μm and adjustment of optical power was made continuously with the imaging depth to address increased scattering and absorption along the optical path-length. An image stack was acquired over a depth of 450 μm.

## 2.3 Graphing of the vessel network

Our two-photon microscopy images of the vascular network have a high contrast-to-noise ratio enabling easy identification of the vascular networks. Rather than employing an automatic segmentation procedure for graphing the vascular network, we manually graph the network

using custom software to accelerate the process. The software enables us to place node points and connecting edges along the vessels. Vessel diameter is estimated at each node by thresholding the image at a low value of approximately 2% of the maximum image intensity, but still above the image noise, considering lines through the node point oriented every 3 degrees in the local  $X$ - $Y$  plane perpendicular to the vessel axis, and finding the minimum distance from vessel edge to vessel edge. At the graph end points we need to establish boundary conditions for velocity or blood pressure. We set the blood pressure boundary condition for the major arterioles and venules and use a zero velocity boundary condition for minor vessel branches that do not connect back to our draining vein. The vascular resistance for each edge between 2 node points is given by Poiseuille's law

$$R = \frac{128\eta l}{\pi d^4}, \quad (18)$$

where  $\eta$  is the viscosity of blood ( $\eta = 15 \times 10^{-6}$  mmHg s [29]),  $l$  is the length of the vessel, and  $d$  is the vessel diameter. Given the resistor network and boundary conditions on blood pressure and velocity, it is straight-forward to solve the set of simultaneous equations for blood pressure and blood velocity at every node point. We follow the procedure we described previously, in [30].

### 3. Results

In this section, we first present our simulation results for a simple vessel network: a single vessel across the tissue. Using these results, we validate our model proposed in the previous section for both steady-state and dynamic simulations. In the second half of this section, we apply our analysis to a more complex vessel network extracted from a two-photon microscopy scan of a rodent somatosensory cortex. These simulations further demonstrate the accuracy and scalability of the proposed model. We note that, while our calculations are for the concentration of oxygen, we report the partial pressure of oxygen ( $PO_2$ ) in our figures as it is commonly reported in experimental papers. The  $PO_2$  is related to the oxygen concentration,  $C$ , by  $PO_2 = C/a$ .

#### 3.1 Validation

The tissue that we are simulating is  $100 \times 100 \times 100 \mu\text{m}^3$  in size and contains a single blood vessel with diameter of  $d = 10 \mu\text{m}$ . The vessel is passing through the center of the tissue and parallel to the  $x$ -axis. Unless otherwise stated, for this simple simulation the velocity of blood inside the vessel is  $400 \mu\text{m/s}$ , hematocrit is set to 0.1, and  $PO_2 = 90$  mmHg at the input boundary of the vessel. The vessel wall permeability is  $K_w = 1.115 \times 10^{-12} \mu\text{mol}/(\mu\text{m s mmHg})$  and wall thickness is  $1 \mu\text{m}$ . The oxygen diffusion coefficient is  $D_{O_2} = 2.4 \times 10^6 \mu\text{m}^2/\text{s}$ . Oxygen consumption is  $41.7 \times 10^{-16} \mu\text{mol}/(\mu\text{m}^3\text{s})$ , or 10% of the baseline value for the rat cortex [31]. A mesh with 25554 nodes and 120942 tetrahedral elements was created using our customized mesh generator. The meshing process took about 14 seconds on a 1.8GHz Intel Xeon (64bit) PC and building the matrices in Eqs. (9) and (16) took about 11 seconds. Subsequently, we solved Eqs. (9), (10) and (16) for about 1.3 seconds per time step.

In Fig. 2(a) we show a contour plot of the steady state  $PO_2$ , obtained for the above simulation parameters in  $X$ - $Y$  plane that contains the vessel axis. We see a high  $PO_2$  for the inflowing blood on the left (starting at 90 mmHg), diminishing as the blood flows across the vessel to a minimum of 64 mmHg indicated by the last contour on the right. In Fig. 2(b), (c), and (d), we plot the  $PO_2$  along the interior of the vessel for various values of the blood velocity, hematocrit, and tissue oxygen consumption, respectively. As we increase velocity from 0.4 mm/s to 0.8



mm/s and 1.6 mm/s, we see that the  $PO_2$  is increasing as more oxygen is being delivered by the blood per unit time, but the oxygen extraction by the tissue is constant, and thus the oxygen extraction fraction is expected to decrease. Similarly, as we increase the hematocrit from 0 to 0.2 we see that  $PO_2$  increases as more oxygen is delivered by the blood. When tissue oxygen consumption is increased, the  $PO_2$  in the blood decreases, as expected. The difference between the oxygen flowing into the volume per unit time and the oxygen flowing out should be equal to the tissue volume integral of the oxygen consumption. Assuming the uniform oxygen consumption (OC, in  $\mu M/s$ ), the oxygen conservation requires

$$\left(\frac{\pi}{4}d^2v\right)(C_{T,in} - C_{T,out}) = V_{tis} OC, \quad (19)$$

where  $v$  is the velocity of blood,  $C_{T,in}$  and  $C_{T,out}$  are the total concentrations of oxygen at the input and output boundaries of the blood vessel, respectively, and  $V_{tis}$  is the tissue volume. The left-hand-side of Eq. (19) denotes the total oxygen extracted from the vessel per unit time while the right-hand-side denotes the quantity of oxygen consumed by the tissue.

To validate the steady-state solution obtained by our finite element model, we calculated the  $PO_2$  distributions under various velocities, hematocrit rates and OC values, and the solutions are shown in Fig. 2. The expected conservation relationship, i.e. Eq. (19), holds for all the steady-state simulations.

The second step is to validate the model for dynamic processes. In these simulations, we separately explored the dynamics of oxygen advection within the vessel, flux across the vessel membrane and diffusion in the tissue and compared the calculations with simple analytic solutions. These results are shown in Fig. 3 and detailed below.

Oxygen advection within the vessel was isolated from oxygen diffusion by setting the vessel wall permeability  $K_w = 0$ . We started with no oxygen in the vessel and introduced 90 mmHg of oxygen pressure at the input of the vessel ramping down to 0 mmHg at 40  $\mu m$  into the vessel. Fig. 3(a) shows the oxygen pressure profiles along the vessel at 20 ms time intervals. We see that the oxygen wavefront is advancing almost 8  $\mu m$  every 20 ms, consistent with the velocity of 0.4 mm/s. It is known that a two-level implicit advection solver produces solutions that underestimate the true velocity at high spatial frequencies and accurately estimate the velocity at low spatial frequencies [26]. This is evident in Fig. 3(a) with smoothing of the edges at 90 mmHg and 0 mmHg as the oxygen advects along the vessel. We note that this is an intrinsic limitation of the discretization scheme, and although we have implemented the most accurate solver, it places limits on the accuracy of our solution for oxygen content varying with high spatial frequency along a vessel. As noted in Ref. [26], this limitation can be reduced by using a refined time step or smaller grid spacing.

Flux of oxygen across the vessel wall was validated by fixing the vessel  $PO_2$  at 90 mmHg, initiating the tissue  $PO_2$  at 0 mmHg, setting the tissue oxygen consumption to 0, and increasing the oxygen diffusion coefficient within the tissue by a factor of 1000 such that the system dynamics would be limited by the vessel wall permeability  $K_w$ . In Fig. 3(b), we plot the tissue temporal evolution of  $PO_2$ , which is increasing to 90 mmHg due to oxygen flux across the permeable vessel wall. When we reduce  $K_w$  by a factor of 2, we see that the rate of increase for the tissue  $PO_2$  is reduced. The rate of change in the total oxygen content of the tissue volume is given by Fick's law [28] as



$$\frac{\partial N_{O_2,tis}}{\partial t} = \pi dl \frac{K_w}{w} (N_{O_2,ves} - N_{O_2,tis}), \quad (20)$$

where  $N_{O_2}$  is the number of moles of oxygen in the vessel or tissue,  $d$  is the diameter of the vessel,  $l$  is the vessel length,  $w$  is the vessel wall thickness, and we assume that any oxygen that crosses the vessel wall distributes uniformly throughout the tissue volume effectively immediately (i.e., the diffusion time constant is much shorter than the vessel wall flux time constant). Under these conditions, the solution of Eq. (20) is a simple exponential. Note that

$$PO_{2,x} = \frac{N_{O_2,x}}{\alpha V_x}, \quad (21)$$

where  $x$  indicates either tissue (*tis*) or vessel (*ves*). The solution of Eq. (21) is shown in Fig. 3 (b) and agrees well with the solution of our finite element model.

Oxygen diffusion was validated by setting oxygen consumption to 0 and initiating the tissue  $PO_2$  to 0 mmHg except for a single volume element far from the boundaries of the tissue volume that was given a unit quantity of oxygen. This oxygen was then diffused with our finite element model. The early responses of diffusion after 20 (blue), 25 (green), and 30 ms (red) are plotted in Fig. 3(c) and they roughly agree with the analytic solution of the diffusion equation for a homogeneous infinite medium. We also computed the finite element solution reducing the diffusion coefficient by a factor of 2 and plot the results at 40 (blue), 50 (green), and 60 ms (red) and observed the expected  $D_{O_2}t$  scaling of the diffusion equation. That is, if we half the diffusion coefficient and double the time, the analytic solution [32] predicts the same solution.

Tissue oxygen consumption was validated by setting  $PO_{2,tis}$  to 90 mmHg throughout the tissue volume, inhibiting oxygen flux across the vessel wall by setting  $K_w = 0$ , and increasing oxygen consumption. Our simulation result (not shown) demonstrates a linear decrease in oxygen concentration in the tissue with time, as we expected.

### 3.2 Application to a microvessel network

After validating the steady state and dynamic solutions of our oxygen advection-diffusion solver, we proceed in solving for the delivery of oxygen to tissue by a realistic microvessel network. We obtain a volumetric image of the microvessel network from the somatosensory cortex of a rat using two-photon microscopy as described in the methods. The volumetric image spanning  $230 \times 230 \times 450 \mu\text{m}^3$  is shown in Fig. 4(a). In this image, we identify a 25  $\mu\text{m}$  in diameter surface pial arteriole in the upper right delivering oxygenated blood to the tissue and a draining ascending venule in the upper left of the image, connected by the intervening capillary network.

We manually graphed this vessel network in under 2 hours using custom software to accelerate the process, by placing node points and connecting edges along the vessels. The diameter of the vessel at each node point, the blood pressure, and velocity of blood was calculated as described in the methods. The velocity at each node in the vascular graph was used in solving the oxygen advection diffusion equation to obtain the partial pressure of oxygen at every node point in the vessels and throughout the tissue. The vessel in-flow and out-flow points (i.e., the boundary points as mentioned in Section 2.1) were manually labeled and used for the subsequent advection modeling. The generated 3D mesh for this case contains 138685 nodes

and 607406 elements. The total time for mesh generation, calculating the matrices and solving for each time step are 136, 62 and 6 seconds, respectively.

In Fig. 4(b) we plot the graphed vascular network identifying the arterioles (red), capillaries (green), and venules (blue). We see that the surface pial arteriole branches twice. The left-hand branch propagates along the surface to the lower left of the image and then descends 450  $\mu\text{m}$  to the bottom of the image without branching. The right-hand branch descends into the tissue at the lower right. This descending arteriole quickly branches a few times leading to a capillary network that connects with an ascending venule on the upper left of the image. The velocity of blood along the vascular network is shown in Fig. 4(c). The velocity has a maximum of 10 mm/s in the pial arteriole and reaches a minimum of  $\sim 1$  mm/s in the capillaries and draining venules. The partial pressure of oxygen along the network is graphed in Fig. 4(d), showing the expected decrease from feeding arteriole to draining venule.

The median velocity, blood pressure, and partial pressure of oxygen versus vessel diameter are shown in Fig. 5. Our pressure distribution compares well with a survey of experimental data [33]. Our velocity and partial pressure of oxygen, however, drop below experimental data [33,34] in the capillaries and venules. This is likely a result of our incomplete vascular graph not accounting for the surrounding microvessels that are providing more blood into the draining vein and delivering more oxygen to the tissue. We will correct this in the future by considering a vascular graph over a larger volume of tissue in order to obtain a more completely connected graph in the central regions.

The partial pressure of oxygen within the tissue is shown in Fig. 6 in slices at different depths and in a movie of the volumetric data. From these data, we see the high tissue  $\text{PO}_2$  around the arterioles dropping off rapidly with distance, while the lower  $\text{PO}_2$  around the capillaries is much more spatially uniform. In Fig. 7 we plot the drop in  $\text{PO}_2$  versus distance from selected arterioles, capillaries, and venules. These results qualitatively agree with experimental *in-vivo* measurements [34].

## 4. Summary

We have described a hybrid numerical algorithm and a general work-flow to model the 3D time-varying oxygen advection diffusion process in an anatomical microvascular network. This framework provides a quantitative and computationally feasible approach for modeling the dynamic processes in the microvessels in the tissue, which is becoming increasingly important in studies of cerebro-vascular physiology and tumor physiology. The proposed algorithm is structurally generic and readily applicable to vessel networks with varying degrees of complexity. The graph representations of the vessel network and finite-element modeling also provide a flexible spatial discretization scheme, which is important to balance computational expense and accuracy. Solving the 3D dynamic diffusion-advection process not only makes this framework useful for modeling tissue oxygen delivery and consumption, but is also extendable to include other molecules such as NO and  $\text{CO}_2$ , or to model the pharmacokinetic processes in drug delivery. Future efforts for this framework include automatic graphing of the vessel network from 3D microscopic images and an in-depth understanding of the stability condition. We will also apply this method to full-sized vessel networks to characterize the microscopic details of oxygen delivery during brain activation and to validate macroscopic NIRS and functional magnetic resonance imaging (fMRI) measurements of oxygen delivery.

## Acknowledgments

The authors would like to acknowledge funding support from NIH R01NS057476, P01NS055104 and R01NS051188, and from the Air Force Office of Scientific Research, Medical Free Electron Laser Program Contract FA9550-07-1-0101. The authors would also like to acknowledge the assistance of Shuai Yuan, Mark Shalinsky, and

Weicheng Wu for *in vivo* experiments, and the help from Wes Turner (Kitware Inc.) and Scott Dineen (OSA) for preparing the interactive datasets.

## References and links

1. Cope M, Delpy DT. System for long-term measurement of cerebral blood flow and tissue oxygenation on newborn infants by infra-red transillumination. *Med Biol Eng Comput* 1988;26:289–294. [PubMed: 2855531]
2. Villringer A, Chance B. Non-invasive optical spectroscopy and imaging of human brain function. *Trends Neurosci* 1997;20:435–442. [PubMed: 9347608]
3. Gibson AP, Hebden JC, Arridge SR. Recent advances in diffuse optical imaging. *Phys Med Biol* 2005;50:R1–43. [PubMed: 15773619]
4. Grinvald A, Lieke E, Frostig RD, Gilbert CD, Wiesel TN. Functional architecture of cortex revealed by optical imaging of intrinsic signals. *Nature* 1986;324:361–364. [PubMed: 3785405]
5. Briers JD. Laser Doppler, speckle and related techniques for blood perfusion mapping and imaging. *Physiol Meas* 2001;22:R35–66. [PubMed: 11761081]
6. Dunn AK, Bolay H, Moskowitz MA, Boas DA. Dynamic imaging of cerebral blood flow using laser speckle. *J Cereb Blood Flow Metab* 2001;21:195–201. [PubMed: 11295873]
7. Villringer A, Them A, Lindauer U, Einhaupl K, Dirnagl U. Capillary perfusion of the rat brain cortex. *Circ Res* 1994;75:55–62. [PubMed: 8013082]
8. Kleinfeld D, Mitra PP, Helmchen F, Denk W. Fluctuations and stimulus-induced changes in blood flow observed in individual capillaries in layers 2 through 4 of rat neocortex. *Proc Natl Acad Sci U S A* 1998;95:15741–15746. [PubMed: 9861040]
9. Plant RL, Burns DH. Quantitative, depth-resolved imaging of oxygen concentration by phosphorescence lifetime measurement. *Applied Spectroscopy* 1993;47:1594–1599.
10. Itzkan I, Qiu L, Fang H, Zaman MM, Vitkin E, Ghiran IC, Salahuddin S, Modell M, Andersson C, Kimerer LM, Cipolloni PB, Lim KH, Freedman SD, Bigio I, Sachs BP, Hanlon EB, Perelman LT. Confocal light absorption and scattering spectroscopic microscopy monitors organelles in live cells with no exogenous labels. *Proc Natl Acad Sci U S A* 2007;104:17255–17260. [PubMed: 17956980]
11. Estrada AD, Ponticorvo A, Ford TN, Dunn AK. Microvascular oxygen quantification using two-photon microscopy. *Opt Lett* 2008;33:1038–1040. [PubMed: 18483504]
12. Wang Y, Bower BA, Izatt JA, Tan O, Huang D. In vivo total retinal blood flow measurement by Fourier domain Doppler optical coherence tomography. *J Biomed Opt* 2007;12:041215. [PubMed: 17867804]
13. Cense B, Chen TC, Nassif N, Pierce MC, Yun SH, Park BH, Bouma BE, Tearney GJ, Boer deJF. Ultra-high speed and ultra-high resolution spectral-domain optical coherence tomography and optical Doppler tomography in ophthalmology. *Bull Soc Belge Ophtalmol* 2006:123–132. [PubMed: 17265794]
14. Wang RK, Jacques S, Ma Z, Hurst S, Hanson S, Gruber A. Three dimensional optical angiography. *Optics Express* 2007;15:4083–4097.
15. Orbach HS, Cohen LB, Grinvald A. Optical mapping of electrical activity in rat somatosensory and visual cortex. *J Neurosci* 1985;5:1886–1895. [PubMed: 4020423]
16. Baker BJ, Kosmidis EK, Vucinic D, Falk CX, Cohen LB, Djuricic M, Zecevic D. Imaging brain activity with voltage- and calcium-sensitive dyes. *Cell Mol Neurobiol* 2005;25:245–282. [PubMed: 16050036]
17. Chance B, Graham N, Mayer D. A time sharing fluorometer for the readout of intracellular oxidation-reduction states of NADH and flavoprotein. *Rev Sci Instrum* 1971;42:951–957. [PubMed: 4398818]
18. Kasischke KA, Vishwasrao HD, Fisher PJ, Zipfel WR, Webb WW. Neural activity triggers neuronal oxidative metabolism followed by astrocytic glycolysis. *Science* 2004;305:99–103. [PubMed: 15232110]
19. Elwell CE, Henty JR, Leung TS, Austin T, Meek JH, Delpy DT, Wyatt JS. Measurement of CMRO<sub>2</sub> in neonates undergoing intensive care using near infrared spectroscopy. *Adv Exp Med Biol* 2005;566:263–268. [PubMed: 16594161]

20. Zheng Y, Johnston D, Berwick J, Chen D, Billings S, Mayhew J. A three-compartment model of the hemodynamic response and oxygen delivery to brain. *Neuroimage* 2005;28:925–939. [PubMed: 16061400]
21. Huppert TJ, Allen MS, Benav H, Jones PB, Boas DA. A multicompartment vascular model for inferring baseline and functional changes in cerebral oxygen metabolism and arterial dilation. *J Cereb Blood Flow Metab* 2007;27:1262–1279. [PubMed: 17200678]
22. Huppert TJ, Allen MS, Diamond GS, Boas DA. Inferring cerebral oxygen metabolism from fMRI with a dynamic multi-compartment Windkessel model. *Human Brain Mapping*. 2008in press
23. Franceschini MA, Thaker S, Themelis G, Krishnamoorthy KK, Bortfeld H, Diamond SG, Boas DA, Arvin K, Grant PE. Assessment of infant brain development with frequency-domain near-infrared spectroscopy. *Pediatr Res* 2007;61:546–551. [PubMed: 17413855]
24. Beard DA, Bassingthwaite JB. Modeling advection and diffusion of oxygen in complex vascular networks. *Ann Biomed Eng* 2001;29(4):298–310. [PubMed: 11339327]
25. Lodbell DD. An invertible simple equation for computation of blood O<sub>2</sub> dissociation relations. *J Appl Physiol* 1981;50(5):971–973. [PubMed: 7228771]
26. Lynch, DR. *Computational Partial Differential Equations for Environmental Scientists and Engineers – A First Practical Course*. Springer; 2005.
27. Godsil, C.; Royle, G. *Algebraic Graph Theory*. Springer-Verlag; 2001.
28. Popel AS, Pittman RN, Ellsworth ML. Rate of oxygen loss from arterioles is an order of magnitude higher than expected. *Am J Physiol Heart Circ Physiol* 1989;256(3 Pt 2):H921–4.
29. Haidekker MA, Tsai AG, Brady T, Stevens HY, Frangos JA, Theodorakis E, Intaglietta M. A novel approach to blood plasma viscosity measurement using fluorescent molecular rotors. *Am J Physiol Heart Circ Physiol* 2002;282:H1609–H1614. [PubMed: 11959622]
30. Boas DA, Jones SR, Devor A, Huppert TJ, Dale AM. A vascular anatomical network model of the spatio-temporal response to brain activation. *Neuroimage* 2008;40(3):1116–29. [PubMed: 18289880]
31. Herman P, Trubel HK, Hyder F. A multiparametric assessment of oxygen efflux from the brain. *J Cereb Blood Flow Metab* 2006;26:79–91. [PubMed: 15973353]
32. Arfken, G. *Mathematical Methods for Physicists*. Vol. 3rd. Orlando, FL: Academic Press; 1985.
33. Lipowsky HH. Microvascular rheology and hemodynamics. *Microcirculation* 2005;12:5–15. [PubMed: 15804970]
34. Vovenko E. Distribution of oxygen tension on the surface of arterioles, capillaries and venules of brain cortex and in tissue in normoxia: an experimental study on rats. *Pflugers Arch* 1999;437:617–623. [PubMed: 10089576]

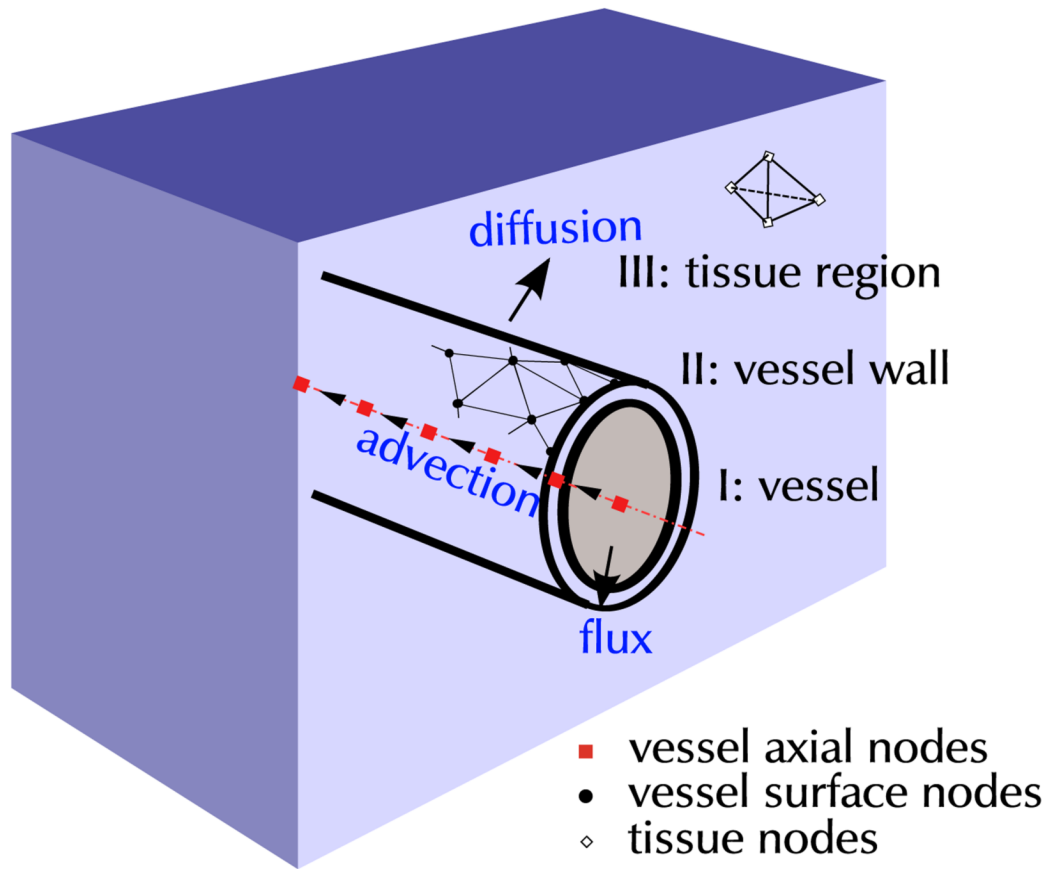


**Fig. 1.**  
The decomposition of the problem domain.

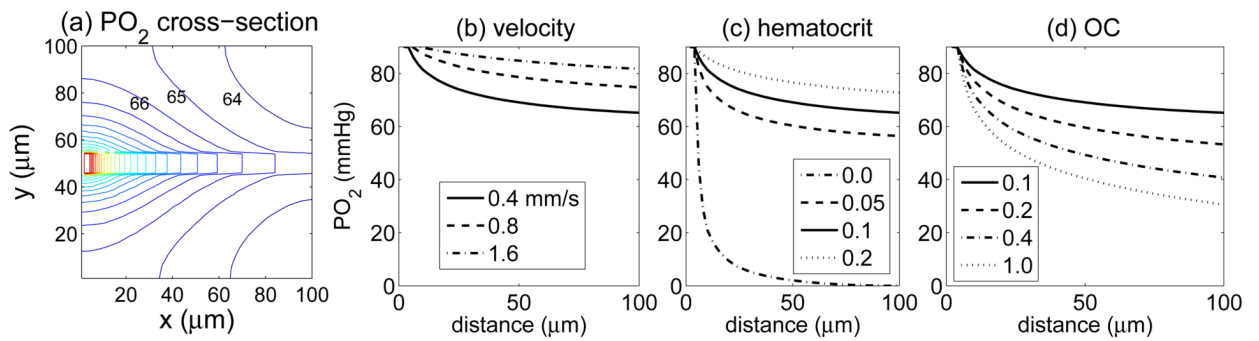


**Fig. 2.** Model validations with a single vessel: (a)  $PO_2$  distribution across an  $X$ - $Y$  plane along the vessel; (b-d)  $PO_2$  along the vessel for different values of (b) blood velocity, (c) hematocrit, and (d) oxygen consumption.

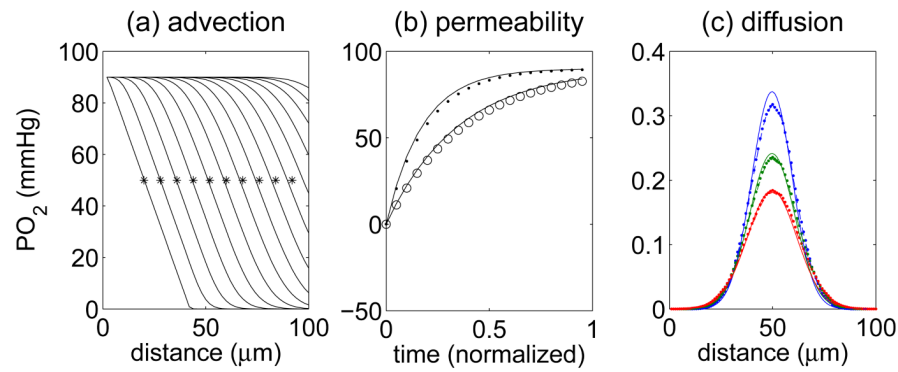


**Fig. 3.** Validation of dynamic processes with a single vessel. (a) PO<sub>2</sub> profiles along the vessel at 20 ms intervals for isolated advection. The modeled PO<sub>2</sub> profile is given by the solid line. The star represents the expected advancement of oxygen pressure profile of 8 μm/s. (b) Tissue PO<sub>2</sub> evolution for validation of vessel wall permeability. The dots and dashed line show our model results for  $K_w$  and  $K_w/2$  respectively, and the solid line is the analytic prediction. (c) Tissue PO<sub>2</sub> profiles at different times for validation of diffusion (see text for more details). The solid line is the analytic solution of the diffusion equation and dots and dashed line are our model results for  $D_{O_2}$  and  $D_{O_2}/2$  respectively.



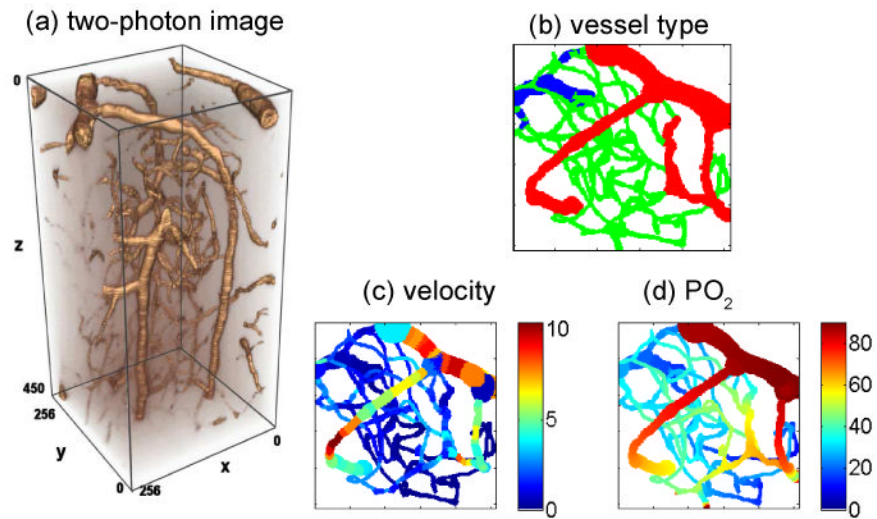


**Fig. 4.** Anatomical vessel network extracted from two-photon scans of a rodent somatosensory cortex. (a) Raw image ([Media 1, View 1](#)). (b-d) Top view projections of the 3D maps of (b) vessel types: arterioles - red, venules - blue, and capillaries - green, (c) blood velocity, and (d) PO<sub>2</sub> inside the vessel network ([Media 2](#)).

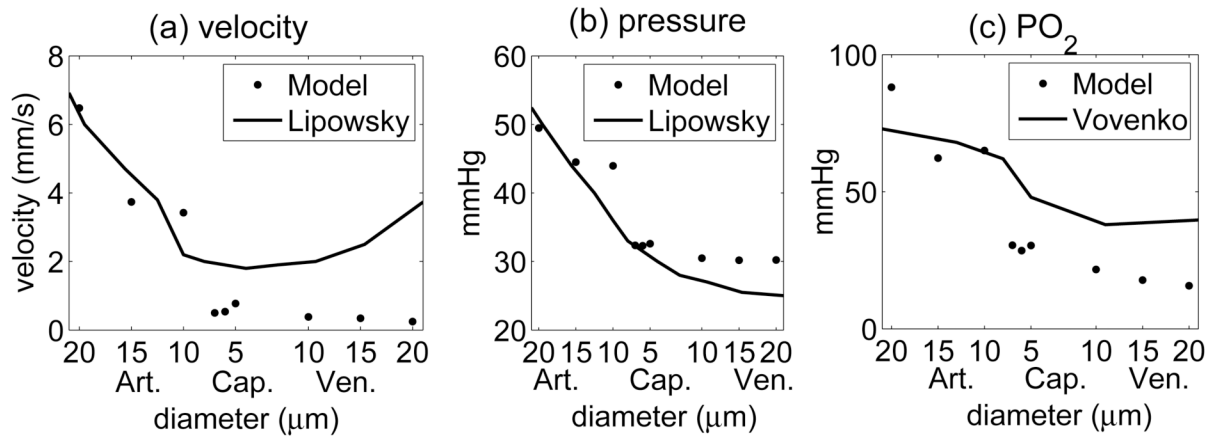


**Fig. 5.** The (a) median velocity, (b) blood pressure and (c) partial pressure of oxygen versus vessel diameter compared with experimental data from the literature. The experimental data in panel (a-b) were derived from [33] and (c) from [34].

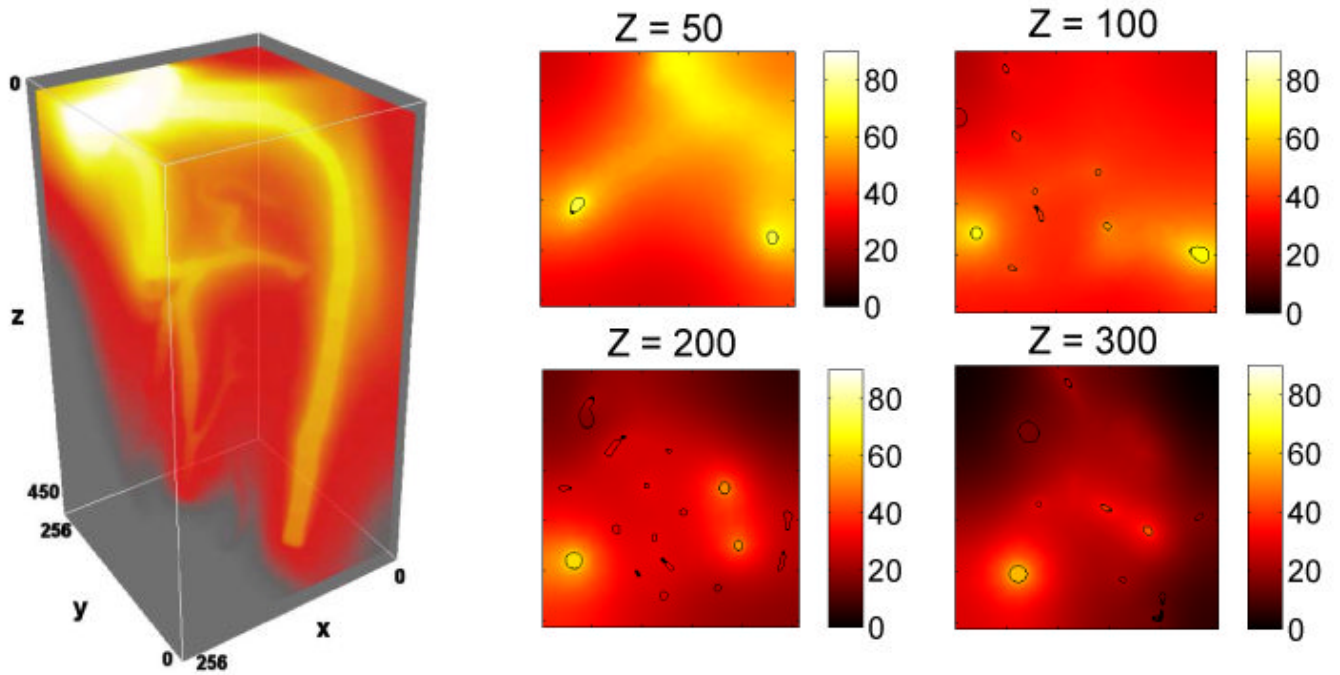


**Fig. 6.** The 3D rendering (left, [Media 3, View 2](#)) and cross-sections (right) of the  $PO_2$  distributions in the vessel and tissue.

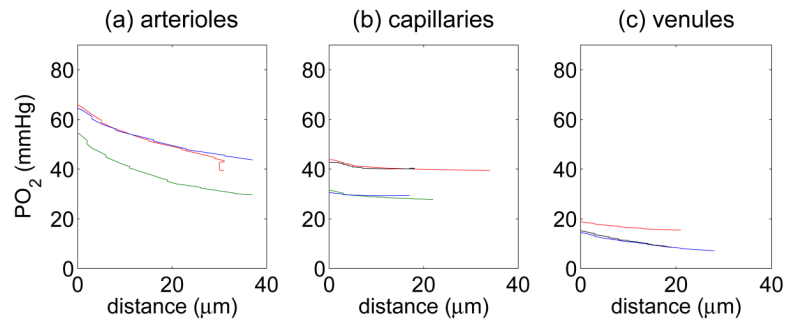


**Fig. 7.** The tissue  $PO_2$  versus distance from a vessel wall of a few selected (a) arterioles, (b) capillaries and (c) venules. Different colors represent different vessels selected for this test.